PHYSICAL REVIEW APPLIED **21,** 054053 (2024)

Exploring the applications of ScXI ($X = $ S, Se, Te) monolayers for microelectronic nanodevices and photoelectric sensors

Juncai Chen,[1] Xiaozheng Fan,[1] Jiajun Li,[1] Chunlan Ma,[2,*] Shijing Gong,[3] Tianxing Wang,[1]
Xiao Dong,[1] Guoliang Xu,[1] and Yipeng An[1,†]

[1] *School of Physics, Henan Normal University, Xinxiang 453007, China*
[2] *School of Physics and Technology, Suzhou University of Science and Technology, Suzhou 215009, China*
[3] *Department of Physics, East China Normal University, Shanghai 200062, China*

(Received 21 February 2024; revised 7 April 2024; accepted 3 May 2024; published 24 May 2024)

Wide-band-gap two-dimensional semiconductors have extensive applications in high-power electronics and optoelectronics in the blue to ultraviolet region. In this study, we investigate the electronic, mechanical, transport, and photoelectric properties of ScXI ($X = $ S, Se, Te) monolayers using a first-principles method. Some conceptual nanodevices based on ScXI monolayers are constructed, such as p-n-junction diodes, field-effect transistors (FETs), and phototransistors. Their multifunctional properties are subsequently revealed. The results indicate that ScXI monolayers, all of which are semiconductors with a moderate direct band gap of 2.42–1.34 eV, show many interesting properties, such as high dynamical, thermal, and mechanical stabilities, low cleavage energy, significant mechanical anisotropy, relatively low stiffness, and electronic properties that are tunable via applying strain. Additionally, the p-n-junction diodes of the ScXI monolayers display a strong rectifying effect and remarkable electrical anisotropy behavior. Moreover, the gate voltages effectively regulate the current through the FETs of the ScXI monolayers. ScXI monolayers and their phototransistors also show good photoelectric responses in the visible and ultraviolet regions. Strain can tune the device transport and photoelectric properties of the ScSI monolayers. Our results suggest that ScXI monolayers can be an alternative platform for flexible applications in microelectronic nanodevices, especially in photoelectric sensors.

DOI: 10.1103/PhysRevApplied.21.054053

I. INTRODUCTION

With the miniaturization of traditional semiconductor devices reaching their physical limit and Moore's law approaching its bottleneck, it is difficult for traditional materials to meet the growing computational requirements of the big data era [1]. Since graphene was discovered in 2004 [2], two-dimensional (2D) materials, such as transition metal dichalcogenides [3–8], h-BN [9,10], black phosphorus [11,12], MXene [13,14], and $MnBi_2Te_4$ [15,16], have attracted extensive attention because of their unique mechanical, thermodynamic, optical, electrical, and magnetic properties. The atomic-level thickness of 2D materials, confining charge and heat transport to a single plane, provides several benefits for applications in next-generation nanodevices [17–21]. Additionally, the electronic transport properties of 2D materials hold significant interest and importance for future nanoscale devices [22–24]. Nevertheless, owing to the inherent shortcomings of some 2D materials, such as the zero band gap in graphene [25,26], low stability in black phosphorus [27], and low carrier mobility in MoS_2 [28,29], their practical applications are limited.

Recently, ternary 2D materials with the FeOCl-type structure have attracted significant interest because of their intriguing electronic, optical, magnetic, and topological properties. Notably, materials such as $Al_2Se_2Y_2$ ($Y = $ Cl, Br, I) [30,31], CrXY ($X = $ O, S, Se; $Y = $ Cl, Br, I) [32–39], and MnNY ($Y = $ Cl, Br, I) [40–43], have demonstrated tunable band gaps, exceptional charge carrier mobilities, and interesting magnetic behaviors. By exploiting their promising attributes, researchers have explored diverse applications, including photovoltaics, optoelectronics, thermoelectrics, and spintronics [31,39,44–46]. However, it is important to note that most of these materials are narrow-band-gap semiconductors with band gaps below 2 eV. This limitation hinders their performance in high-power electronics and optoelectronics in the blue to ultraviolet region (UR), where materials with wide band gaps are required [47]. Ferrenti *et al.* [48] successfully synthesized a new exfoliatable semiconductor from bulk ScSI with an indirect optical band gap of 2.0 eV, and its corresponding 2D monolayer is predicted to have

---

[*] Corresponding author: wlxmcl@mail.usts.edu.cn
[†] Corresponding author: ypan@htu.edu.cn

an indirect band gap of approximately 2.7 eV using the hybrid functional (HSE06) approach [46,49,50]. In addition, monolayer ScXY ($X =$ S, Se; $Y =$ Cl, Br, I) has been theoretically proven to have high stability, strong anisotropic properties, and good thermoelectric performance [46,49,50]. These properties indicate that ScXY nanosheets have potential applications in nanodevices for field-effect transistors (FETs), photodetectors, and phototransistors in the blue to ultraviolet region. However, studies on the transport properties of ScXY monolayers, such as electronic transport and photoelectronic properties, are scarce.

In this study, we focused on the transport properties of wide-band-gap 2D ScXI ($X =$ S, Se, Te) semiconductors. Several conceptual nanodevices, including *p*-*n*-junction diodes, FETs, and phototransistors, were constructed based on these monolayers, and their electronic transport performances and photoelectronic characteristics were thoroughly investigated. The structural stability, electronic structures, electronic transports, and photoelectronic properties of the ScXI monolayers were systematically investigated. Strain engineering has emerged as a highly effective and popular technique for precisely tuning the electrical, superconducting, magnetic, optical, and transport properties of 2D materials. To broaden the potential applications of these materials, we employed strain engineering on the ScSI monolayer to explore the electrical properties, especially the electronic transport and photoelectronic properties. The remainder of this paper is organized as follows. First, the geometric structure and structural stability of ScXI monolayers are demonstrated. Second, the electronic structures and properties of the ScXI monolayers are systematically investigated. Third, a brief investigation of the effects of strain on the electronic properties of the ScSI monolayers is presented. Finally, several conceptual ScXI-based nanodevices, including *p*-*n*-junction diodes, FETs, and phototransistors are constructed to investigate electronic transport properties and photoelectronic properties of ScXI monolayers.

II. CALCULATION METHODS

Here, we focus on the geometric and electronic structure and the transport properties of several conceptual nanodevices such as *p*-*n*-junction diodes, FETs, and phototransistors of ScXI monolayers. All calculations were performed within the density-functional theory (DFT) framework combined with the nonequilibrium Green's function [51] method, as implemented in the QUANTUMATK code [52]. The generalized gradient approximation of the Perdew-Burke-Ernzerhof (PBE) functional [53] was adopted to describe the exchange-correlation interactions. The van der Waals correction proposed by the DFT-D3 [54,55] approach in Grimme's scheme was chosen to describe the intralayer long-range interactions. Considering the strong correlation of the Sc 3d orbital electrons, PBE + U calculations were applied in this study as a correction to the PBE. The value of the optimal on-site Hubbard U was determined by comparison with the experimental band gap. When the Hubbard U value was 4 eV, the obtained band gap of the bulk ScSI was 2.008 eV, which is consistent with the previously reported experimental values (2.0 eV) [48]. Therefore, the Hubbard U was set to 4.0 eV throughout this study. The electron wave functions were expanded using linear combination of atomic orbitals basis sets with a real-space grid density mesh cutoff of 100 hartree. Optimized norm-conserving Vanderbilt pseudopotentials of the SG15 type [56] were employed to describe the core electrons. Structural relaxation was considered to converge when the residual forces on each atom were less than 0.001 eV Å^{-1}. Further, the total energy convergence threshold was set to 10^{-6} eV. To avoid interactions between adjacent layers, a vacuum spacing of approximately 30 Å was added along the perpendicular direction of the 2D surface. To investigate the thermal stability, we performed *ab initio* molecular dynamics (AIMD) simulations using the Nosé-Hoover thermostat scheme in the *NVT* ensemble at 300 K with a total simulation time of 5 ps and time step of 1 fs. The Brillouin zone was sampled using $1 \times 6 \times 300$ (X-type) and $8 \times 1 \times 200$ (Y-type) k-point meshes generated via the Monkhorst-Pack scheme [57] for the electrodes of the ScXI monolayer device.

III. RESULTS AND DISCUSSION

A. Crystal structure and stability

Bulk ScSI has a layered orthorhombic structure (space group *Pmmn*, no. 59) belonging to the FeOCl structure type [48]. The optimized lattice constants of ScSI are $a = 3.903$ Å, $b = 5.084$ Å, and $c = 8.623$ Å, which are in good agreement with the previously reported experimental values ($a = 3.8904$ Å, $b = 5.0732$ Å, and $c = 8.9574$ Å) [48] and theoretical values ($a = 3.90$ Å, $b = 5.06$ Å, and $c = 8.99$ Å) [58]. It has been proven that ScSI monolayers can be easily obtained by mechanical exfoliation using the Scotch-tape method [48]. The exfoliation energy of the ScSI monolayer calculated using DFT is 0.22 J m^{-2} [58,59], and that of the ScSeI monolayer is 0.23 J m^{-2} [59], which is close to that of a CrOCl sample (0.21 J m^{-2}) [32] that had been successfully prepared experimentally [44], and significantly smaller than the experimentally estimated value for graphene (0.37 J m^{-2}) [60]. These results demonstrate the feasibility of the experimental preparation of this type of material through mechanical exfoliation.

The ground-state structure of the ScXI monolayers with a fully relaxed geometry is shown in Fig. 1(a). The unit cell includes six atoms: two Sc atoms, two S atoms, and two I atoms, which belong to the rectangular Bravais lattice with the *Pmmn* space group. The calculated structural parameters and previously reported values for the ScXI

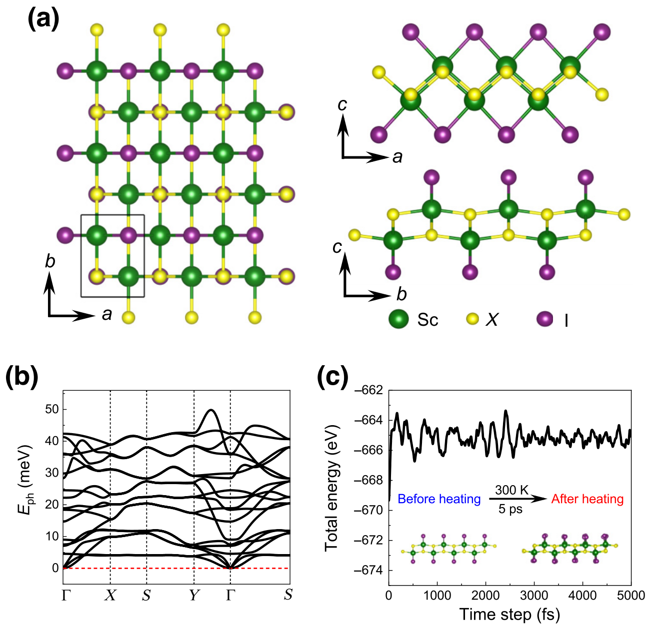

FIG. 1. (a) Top (left) and side (right) views of the atomic structures for ScXI monolayers. The black rectangle with the Bravais lattice vectors is the corresponding unit cell. (b) Phonon spectra of the ScSI monolayer. (c) *Ab initio* molecular dynamics (AIMD) simulation of time-dependent total energy fluctuations at 300 K of the ScSI monolayer. The insets are the side view before and after the AIMD simulation.

TABLE I. The calculated lattice constants a and b, and band gap E_g of the ScXI monolayers. D and I denote whether the band gap is direct or indirect, respectively.

System	a (Å)	b (Å)	E_g (eV)	Reference
ScSI	3.911	5.117	1.708 (PBE) (I)	This work
	3.943	5.134	2.421 (PBE + U) (D)	This work
	3.90	5.08	1.71 (PBE) (D)	Ref. [61]
	3.91	5.07	1.78 (PBE) (D)	Ref. [58]
	3.90	5.08	1.71 (PBE), 2.69 (HSE06) (D)	Ref. [49]
	3.886	5.045	2.15 (HSE06) (I)	Ref. [59]
	3.87	5.048	1.70 (PBE), 2.70 (HSE), 2.59 (HSE06 + SOC) (I)	Ref. [50]
ScSeI	4.001	5.425	2.080 (PBE + U) (D)	This work
	3.96	5.37	1.47 (PBE) (I)	Ref. [61]
	3.948	5.320	1.83 (HSE06) (I)	Ref. [59]
	3.98	5.39	2.50 (HSE06) (I)	Ref. [46]
ScTeI	4.114	5.917	1.344 (PBE + U) (D)	This work

monolayers are summarized in Table I. The relaxed lattice constants of the ScSI monolayer are $a = 3.943$ Å and $b = 5.134$ Å (PBE + U), which are in good agreement with the previously reported data [49,50,58,59,61]. Our results also show that the lattice constants of the ScXI monolayers (Table I) increase as the size of element X increases from S to Te.

The structural stabilities of the ScXI monolayers can be determined by examining their dynamic, thermal, and mechanical properties. Specifically, we calculated the phonon dispersions, AIMD simulations, and elastic constants to evaluate their dynamic, thermal, and mechanical stabilities. As shown in Figs. 1(b) and S1 in the Supplemental Material [62], the phonon spectra of all three ScXI structures exhibit no negative frequencies throughout the Brillouin zone, indicating that the ScXI monolayers are dynamically stable under equilibrium conditions.

The thermal stabilities of the ScXI monolayers were examined using AIMD simulations at room temperature (300 K). Simulations were performed using a 5 × 4 × 1 supercell. Figures 1(c) and S2 in the Supplemental Material [62] show that the atomic structures of the ScXI monolayers remained robust after 5 ps of heating. No remarkable distortions, bond breaking, or structural transitions were observed in the atomic structures of ScXI monolayers, as shown in the snapshots of the crystal structures. The total energies of the ScXI monolayers fluctuated around a certain constant magnitude for AIMD at 300 K, indicating their thermal stability at room temperature.

We further examined the mechanical stability of ScXI monolayers by calculating their elastic constants. The elastic constants ${C_{ij}}^{3\text{D}}$ of the bulk materials were obtained from DFT calculation by using QUANTUMATK code. To evaluate the 2D case, it was necessary to convert the three-dimensional (3D) ${C_{ij}}^{3\text{D}}$ tensor (gigapascals) obtained for a bulk unit cell into a 2D ${C_{ij}}^{2\text{D}}$ tensor (newtons per meter). This can be achieved by multiplying ${C_{ij}}^{3\text{D}}$ by the vacuum thickness h added along the c axis to avoid periodic interactions [63]; that is, ${C_{ij}}^{2\text{D}} = h{C_{ij}}^{3\text{D}}$, where h is the lattice parameter along the c axis (36 Å in this study). The calculated elastic constants (ignoring the out-of-plane thickness and considering only the in-plane case) (Table S1 in the Supplemental Material [62]) of the ScXI monolayers meet the Born criteria [64,65] of $C_{11} > 0$, $C_{66} > 0$, and $C_{11}C_{22} > C_{12}^2$, which implies that they are mechanically stable in the rectangular lattice. To further explore the mechanical properties and elastic anisotropy of ScXI monolayers, the orientation-dependent Young's modulus $E(\theta)$, shear modulus $G(\theta)$, and Poisson's ratio $\nu(\theta)$ were plotted in Fig. 2, where $\theta \in [0°\text{–}360°]$ is the angle with respect to the $+x$ axis. The maximum and minimum of $E(\theta)$, $G(\theta)$, and $\nu(\theta)$ for the ScXI monolayers were also calculated and are summarized in Table S1 in the Supplemental Material [62]. The calculation method for the orientation-dependent elastic moduli and equations are listed in the Supplemental Material [62]. The results show that the Young's modulus, shear modulus, and Poisson's ratio vary with the angle, showing significant mechanical anisotropy for ScXI monolayers and agreeing with previous results [50,59]. The values of $E(\theta)$ and $G(\theta)$ for ScXI monolayers decrease from S to Te, indicating decreasing stiffness. Moreover, compared with other typical 2D materials, the values of Young's modulus $E(\theta)$ are comparable with that of black phosphorene (29–90 N m^{-1}) [65], but remarkably smaller than that of MoS$_2$ (122 N m^{-1}) [65] and graphene (339 N m^{-1}) [65]. These values ensure the mechanical flexibility of the ScXI monolayers and are beneficial for the electronic structure transitions induced by external strain [66]. The ScXI monolayers have a positive Poisson's ratio [Fig. 2(c)], and the maximum and minimum values are along the diagonal direction and x axis, respectively, exhibiting remarkable anisotropy. In addition, the minimum values decrease with increasing atomic weight from S to Te without a significant change in the maximum value, indicating enhanced anisotropy from S to Te.

B. Electronic properties and strain engineering

The element-projected electronic band structures and density of states of the ScXI monolayers were calculated along the Γ-X-S-Y-Γ-S high-symmetry direction. The results shown in Figs. 3(a), 3(c), and 3(e) demonstrate the influence of different atoms on the formation of bands in the energy and momentum space. The ScSI, ScSeI, and ScTeI monolayers exhibited semiconducting characteristics. The band gaps calculated using PBE + U ($U = 4$ eV) agree well with previously reported results (Table I). In addition, we observed that the band gap decreased as the chalcogen atoms moved from S to Te in the ScXI monolayers; that is, $E_g^{\mathrm{ScSI}} > E_g^{\mathrm{ScSeI}} > E_g^{\mathrm{ScTeI}}$. Focusing on the band structures of the ScXI monolayers, as presented in Figs. 3(a), 3(c) and 3(e), both the VBM and conduction band minimum (CBM) of the ScXI monolayers are located at the Γ point. The conduction bands of the ScXI monolayers are primarily determined by the Sc atoms, whereas the contribution of atoms to the formation of the valence bands near the Fermi level varies with the chalcogen atoms moving from S to Te in the ScXI monolayers. The ScSI valence bands are mostly contributed by the I atoms, together with some contributions from the S atoms. Both I and Se atoms contribute remarkably to the valence band of ScSeI, whereas the valence bands of ScTeI are mostly contributed by the Te atoms. The contribution of X atoms to the formation of valence bands near the Fermi level gradually overtakes that of I atoms as the chalcogen atoms move down from S to Te in the ScXI monolayers. Figures 3(b), 3(d), and 3(f) showcase 3D representations that provide visual insights into the characterization of band dispersions near the Fermi energy in ScXI monolayers. These visualizations specifically highlight the top of the valence band and bottom of the conduction band, as well as their corresponding 2D projections within the first Brillouin zone. The electronic bands near the Γ point, especially for the conduction band, exhibit quite flat dispersions along the Γ-Y direction. However, they are very sharp along the Γ-X direction, especially for the valence band. These indicate anisotropy of energy dispersions near the Γ point, thus leading to a large effective mass for holes and electrons near the Γ point along the Γ-Y direction and a relatively smaller effective mass along the Γ-X direction. Furthermore, the valence band states seem to be more dispersive than the conduction band for both Γ-X and Γ-Y directions. This results in the effective mass of holes being smaller than that of electrons along these two directions. The band structures of these materials exhibit substantial variation in energy dispersion, suggesting that the effective masses of both holes and electrons, as well as the carrier mobility, may differ in different directions.

The effective mass $m^*_{e(h)}$ of carriers in the transport direction was measured from the electronic band structure using the formula

$$m^*_{e(h)} = \pm \hbar^2 \left(\frac{d^2 E_k}{dk^2} \right)^{-1}. \tag{1}$$

The value of d^2E_k/dk^2 was obtained by a finite-difference (FD) method of band energy E_k versus reciprocal vector k. $\hbar$ is the reduced Planck constant. More details on the FD method are shown in Supporting Information [62]. The

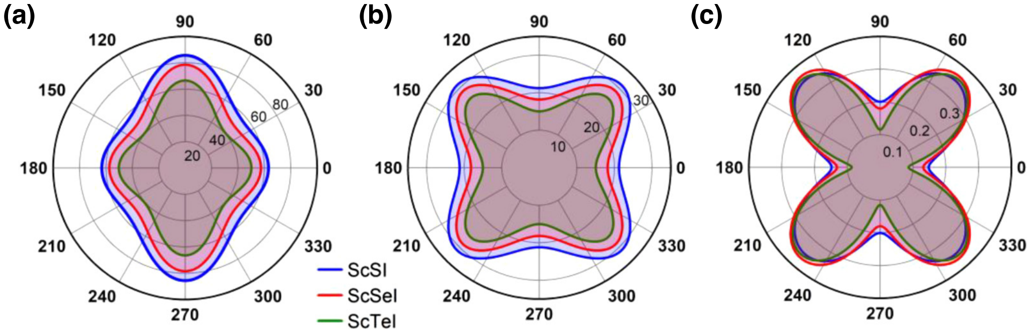

FIG. 2. Calculated orientation-dependent (a) Youngs's modulus $E(\theta)$, (b) shear modulus $G(\theta)$, and (c) Poisson's ratio $\nu(\theta)$ for ScXI monolayers. The $E(\theta)$ and $G(\theta)$ are in units of N m^{-1}, and the angles are in units of degree.

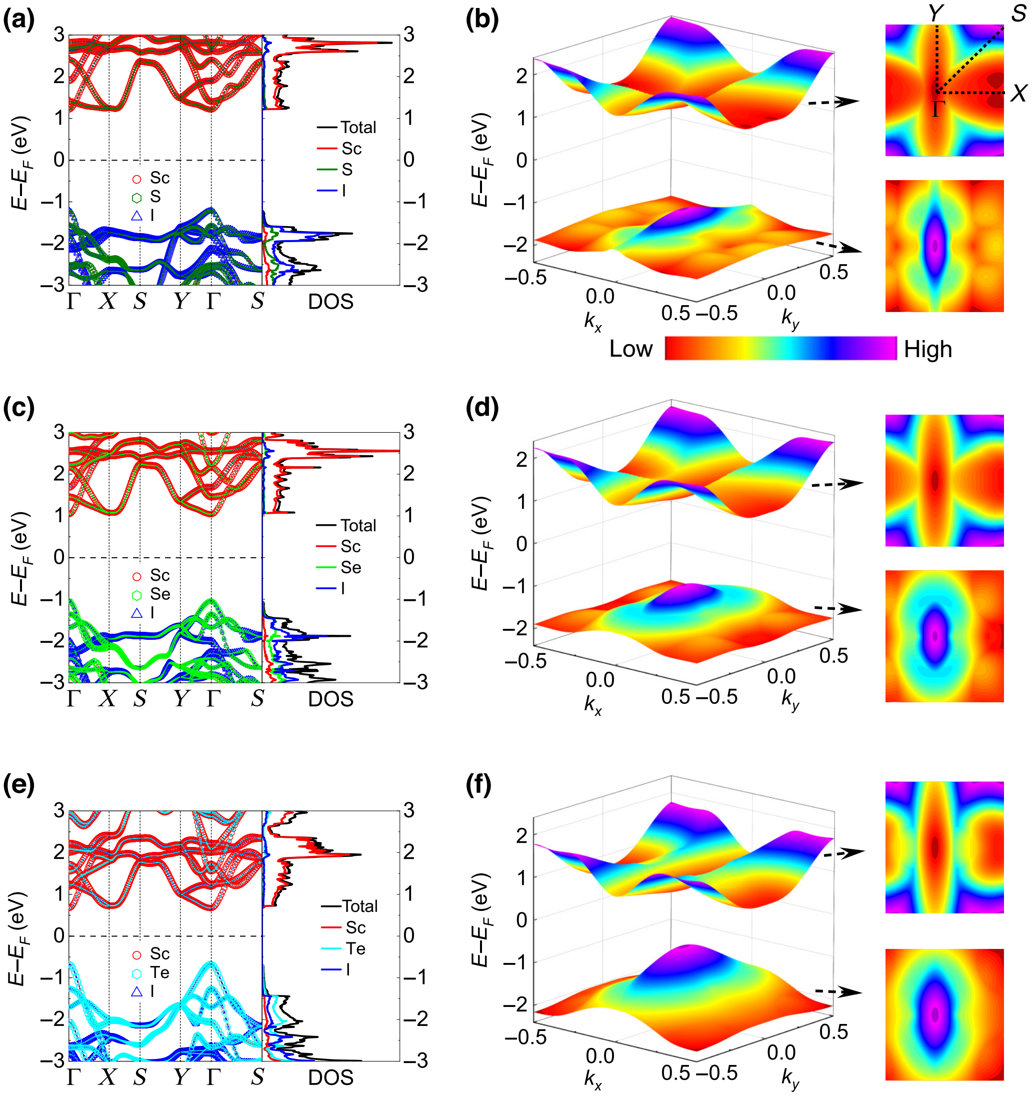

FIG. 3. Element-projected electronic bands and density of states for the (a) ScSI, (c) ScSeI, and (e) ScTeI monolayer. 3D views of the top of the valence band and bottom of the conduction band, and 2D projections in the first Brillouin zone for the corresponding (b) ScSI, (d) ScSeI, and (f) ScTeI.

carrier types e and h denote electron and hole, respectively. The calculated effective masses along the x and y directions are $0.316m_e$ ($0.229m_e$) and $1.497m_e$ ($0.964m_e$) for electrons (holes) at the Γ point for the ScSI monolayers, respectively. m_e denotes the mass of a free electron. The effective masses (both electron and hole) along the x direction are smaller than those along the y direction. Furthermore, the hole effective masses are smaller than electron effective masses for both x and y directions. These results are in agreement with the anisotropic band dispersions in 3D views of the VBM and CBM around the Fermi level [Figs. 3(b), 3(d), and 3(f)]. Based on this analysis, the ScSI monolayer has a relatively small effective mass, which facilitates the carrier transport, except for the value $1.497m_e$ (for electrons) along the y direction, which is in agreement with a quite flat conductive band along this direction. Furthermore, the effective masses of the electrons (holes) for the ScSeI monolayer at the Γ point along the x and y directions are $0.299m_e$ ($0.228m_e$) and $1.532m_e$ ($0.627m_e$), respectively. The effective masses of the electrons (holes) along the x and y directions of the ScTeI monolayer are $0.254m_e$ ($0.194m_e$) and $1.541m_e$ ($0.471m_e$), respectively. These results have similar characteristics and trends to those of the ScSI monolayer. It is expected that the transport properties of ScXI monolayers will show anisotropy in different directions.

Strain manipulation has the potential to significantly alter the electrical characteristics of 2D nanomaterials [67–71] owing to their high susceptibility to structural imperfections. In this regard, we specifically focused on the ScSI monolayer and investigated how its band structure responded to different types of strains. We applied both

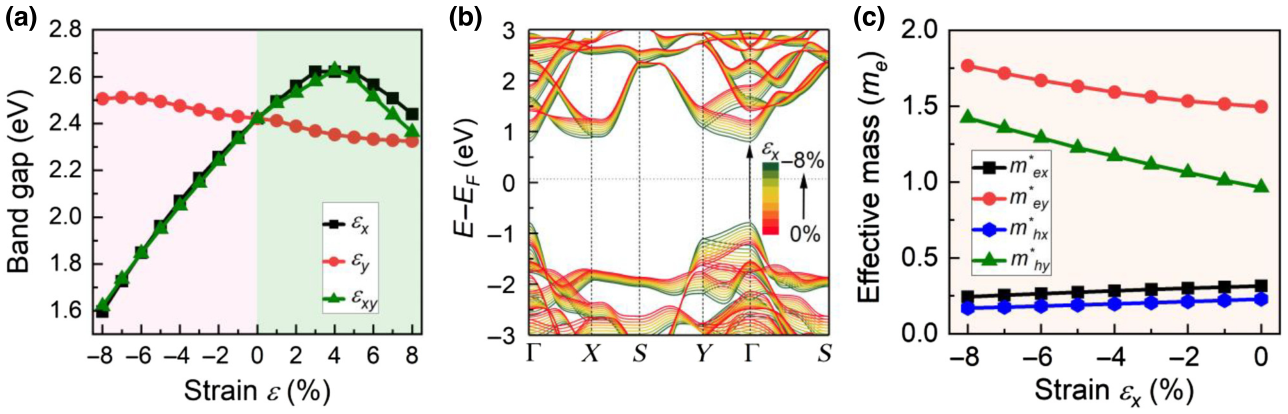

FIG. 4. (a) The band gap of the ScSI monolayer as a function of applied strain ε (uniaxial and biaxial). (b) Band structures under uniaxial compressive strain along the *x* direction. The color map indicates the strain strength. (c) Effective mass of electrons (holes) in the ScSI monolayer as a function of applied uniaxial compressive strain ε along the *x* direction.

uniaxial and biaxial strains along the *x* and *y* directions (corresponding to the orthogonal lattice vectors *a* and *b*), represented as ε_x, ε_y, ε_{xy}, within the range –8% to 8%. The strain is defined as $\varepsilon_x = (a - a_0)/a_0$ and $\varepsilon_y = (b - b_0)/b_0$, where *a* (*b*) and a_0 (b_0) are the lattice constants of the strained and strain-free structures, respectively. Note the structure is relaxed again under strain. The tensile (compressive) strain is represented by a positive (negative) value. First, the phonon dispersions and AIMD calculations at 300 K of the strained structures of the ScSI monolayer were performed (Figs. S3 and S4 in the Supplemental Material [62]), indicating their dynamic and thermal stabilities, respectively. The variations in the band gap with strain and the band structure of the ScSI monolayer with different strains were then plotted in Figs. 4(a), 4(b), and S5 in the Supplemental Material [62]. Our calculations demonstrate that the semiconducting characteristics of the ScSI monolayer were still preserved in the strain range of −8% to 8%. Under tensile strain from 0% to 8%, for both uniaxial *x* and biaxial *xy*, the band gap initially increased, reached a maximum at $\varepsilon = 4\%$, and then decreased. However, the band gap decreased slightly along the uniaxial *y*. In addition, a direct-indirect band-gap transition was brought about at $\varepsilon_{xy} = 1\%$, $\varepsilon_x = 6\%$, and $\varepsilon_y = 1\%$. For example, an indirect band gap appeared at tensile biaxial strain $\varepsilon_{xy} \geq 1\%$ when moving the CBM from the Γ point to the point on the *X*-*S* path and with the VBM remaining at the Γ point. When compressive strain was applied along uniaxial *x* and biaxial *xy* from zero to −8%, the band gap of the ScSI monolayer monotonously decreased, whereas the band gap increased slightly along uniaxial *y*. In the tested compressive strain range, the direct band gap at Γ was preserved. The band gap showed a higher dependence on compressive strain than on tensile strain.

The decrease (increase) in band gap with increasing compressive strain along uniaxial *x* (uniaxial *y*) was also consistent with the energy shift of the band-edge states, as shown in Fig. 4(b). Taking the uniaxial *x* compressive strain case as an example, when compressive strain was applied, the CBM shifted downwards slightly (energy decreased), and the VBM shifted upward (energy increased), leading to a smaller band gap. The effective masses of the electron and hole carriers in the ScSI monolayer as a function of the uniaxial compressive strain along the *x* direction are shown in Fig. 4(c). The effective mass of both electrons and holes along the *x* direction decreased slightly when applying compressive strain ε_x from 0% to −8%, whereas along the *y* direction, it increased. This implies the potential for stronger anisotropic characteristics of carrier migration by applying an external strain.

C. Transport properties of Sc*X*I monolayer *p*-*n*-junction diodes

As mentioned previously, Sc*X*I monolayers are expected to show good transport behavior along *x* and *y* directions due to their small effective mass and relatively high carrier mobilities along the Γ-*X* and Γ-*Y* directions. In addition, using strain engineering to tune the transport and photoelectric properties of the devices may yield interesting results. In this study, we employed an electrostatic doping technique [72] to fabricate *p*-*n*-junction diodes using relaxed Sc*X*I monolayers and strained ScSI monolayers. To achieve this, the compensation charges of the *p*- and *n*-type atoms were incorporated. The transmission direction was served by the *x* and *y* directions of the crystal structures. Figure 5(a) shows a schematic representation of the *p*-*n*-junction diode, which consists of drain (*D*) and source (*S*) electrodes, as well as the central scattering region (*p*-*n* junction). In our transport calculations, the *D* and *S* electrodes were represented using supercells of *p*- and *n*-doped Sc*X*I monolayers, respectively. This supercell extended infinitely in the direction of transmission. When a forward

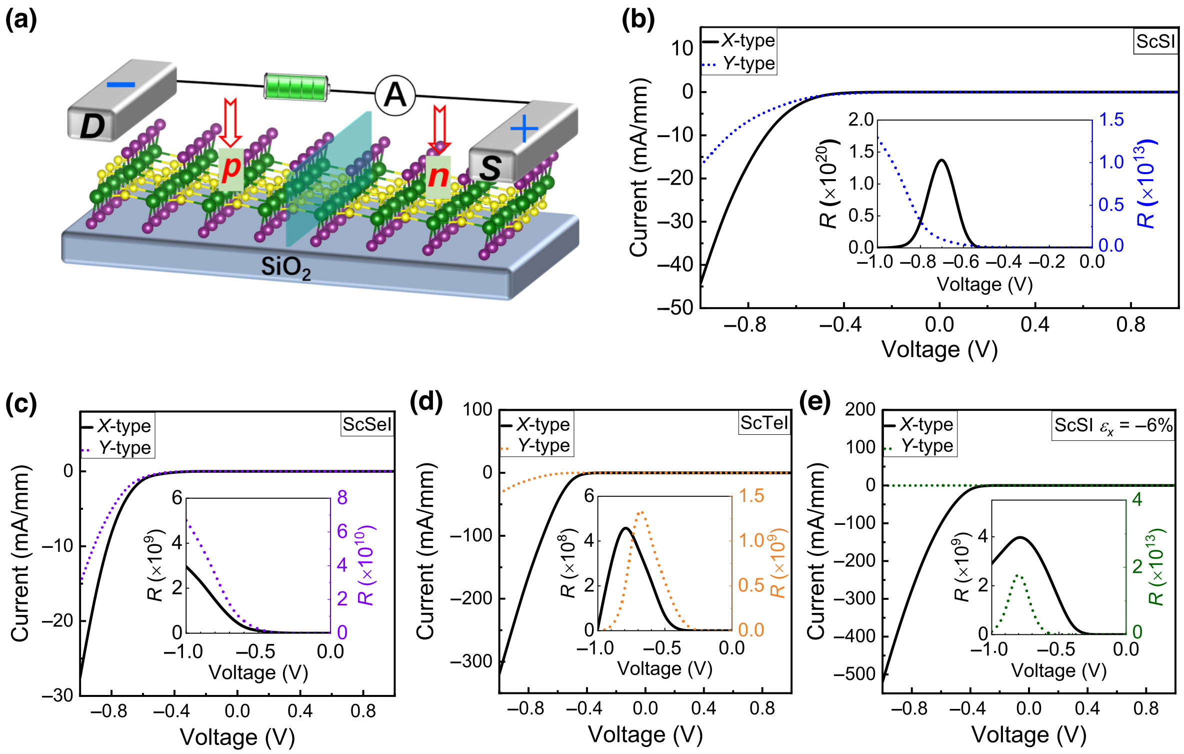

FIG. 5. Transport properties of X-type and Y-type p-n-junction diodes of ScXI monolayers with a doping concentration of 3×10^{13} cm^{-2}. (a) Schematic of the p-n-junction diode. (b)–(d) Bias-dependent current of the p-n-junction diode for ScXI, and (e) ScSI with uniaxial 6% compressive strain along the x direction. The rectification ratio is shown in the inset.

D-S bias of V_b was applied, a positive current flowed from the D electrode to the S electrode, and vice versa. The currents of the p-n-junction diode were calculated by [73]

$$I(V_b) = \frac{2e}{h}\int_{-\infty}^{\infty} T(E, V_b)[F_D(E-\mu_D) - F_S(E-\mu_S)]dE, \tag{2}$$

where e and h represent the electron charge and Planck's constant, respectively, $T(E, V_b)$ is the transmission coefficient, and $F_{D(S)} = \{1 + \exp[E - \mu_{D(S)}/k_B T_{D(S)}]\}^{-1}$ is the Fermi-Dirac distribution function of the D (S) electrode with chemical potential $\mu_{D(S)}$ and temperature $T_{D(S)}$. k_B is the Boltzmann constant. The broadening of the Fermi-Dirac distribution function is typically chosen to be between 0.01 and 0.1 eV. We used the QUANTUMATK default value of 0.026 eV throughout this study, which is equivalent to 300 K. In this work, the bias voltage range was from -1 to 1 V with a sampling interval of 0.1 V.

Based on the atomic geometry, there are two possible ScXI monolayer diode structures: X type (along the x axis) and Y type (along the y axis). We investigated the transmission performance of the p-n-junction diodes under a medium doping concentration of 3×10^{13} cm^{-2}, corresponding to 1×10^{20} cm^{-3} in the bulk, according to the typical doping concentration range of 10^{19}–10^{21} cm^{-3} in the bulk [24,72]. Figure 5(b) shows the current versus bias voltage (I-V) curves of the X- and Y-type ScSI-monolayer p-n-junction diodes. Both X- and Y-type diodes exhibited excellent unidirectional transport features.

That is, the electrical current remained almost zero (circuit-off state) under a limited whole forward bias range but was turned on (circuit-on state) when the reverse bias voltage was larger than the threshold voltage (approximately -0.6 V for both types of diodes). Furthermore, the rectification ratio (R), defined as $R = |I(-V_b)/I(V_b)|$, had a magnitude of up to 10^{20} (10^{13}) for the X-type (Y-type) ScSI-monolayer-based diode, much larger than those of some lateral heterojunctions and 2D material p-n junctions [16,19,74,75]. In addition, the current densities of X-type (I_X) p-n-junction diodes were larger than those of Y-type (I_Y) diodes, demonstrating remarkable electrical anisotropy. The current anisotropy ratio η, defined as $\eta = I_X/I_Y$, was 2.59, which is much greater than that of other 2D materials [16], implying strong anisotropy. The differential conductance (dI/dV) density curves as a function of bias for the X- and Y-type ScSI-monolayer p-n-junction diodes [Fig. S6(a) in the Supplemental Material [62]] also show the strong electrical anisotropy of the ScSI monolayer. Compared with

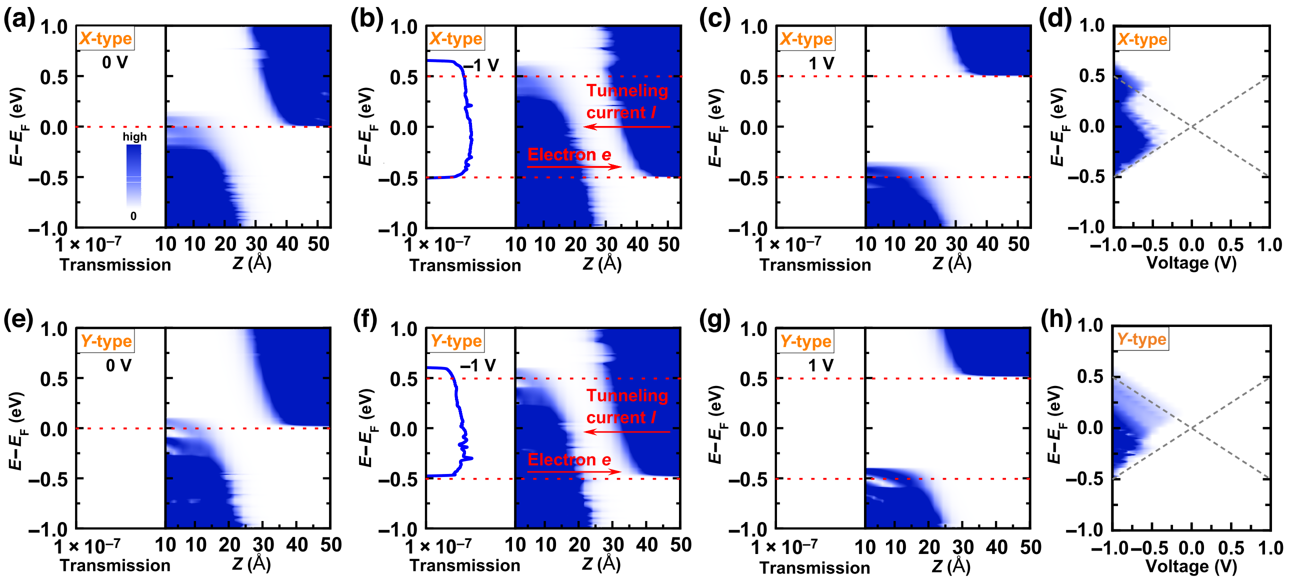

FIG. 6. Transmission coefficient $T(E)$ and projected local density of states (PLDOS) of X-type and Y-type p-n-junction diodes of the ScSI monolayer under biases of 0 V (a),(e); −1 V (b),(f); and 1 V (c),(g). Transmission spectra $T(E, V)$ of X-type and Y-type p-n-junction diodes (d),(h). Color map in (a) shows data from 0 (white) to high (blue) for (a)–(h).

the ScSI-monolayer-based diode, the ScSeI- and ScTeI-monolayer-based diodes also showed a similar perfect rectification effect with a considerably high rectifying ratio at least up to 10^8, as shown in Figs. 5(c), 5(d), S6(b), and S6(c) in the Supplemental Material [62]. Interestingly, compared with the ScSI-monolayer-based diode, it is notable that the ScTeI-monolayer-based diode exhibited a significantly higher current density, especially up to 319.45 mA mm^{-1} at the bias of −1.0 V for X-type diodes, slightly higher dI/dV density, and a slightly lower threshold voltage (approximately −0.5 V for X-type diodes). This is mainly due to the smaller band gap and effective mass of the ScTeI monolayer, which lead to a lower energy barrier and easy carrier migration. Moreover, the ScTeI monolayer also revealed stronger electrical anisotropy [Figs. 5(d) and S6(c) in the Supplemental Material [62]] with a greater current anisotropy ratio ($\eta = 9.65$). Figure 5(e) displays the I-V curves of the p-n-junction diodes based on the strain-engineered (with 6% compressive strain in the x direction) ScSI monolayer. Compared with the strain-free case, when applying 6% compressive strain along the x direction, a perfect rectification effect with a considerably high rectifying ratio was preserved. Furthermore, the current density can be tuned dramatically via applying external strain; that is, the current density of X-type diodes increased dramatically, especially as high as 519.45 mA mm^{-1} at the bias of −1.0 V, which is approximately 10 times larger than that of the strain-free case. In comparison, a reduction in the current density appeared for Y-type diodes, as low as 0.417 mA mm^{-1} at the bias of −1.0 V, which is approximately 40 times lower than the strain-free case, thus resulting in extremely strong electrical anisotropy with a great current anisotropy ratio ($\eta = 1244.96$). Furthermore, strain engineering induced a lower threshold voltage, approximately −0.4 V for X-type diodes, and a dI/dV density increase of approximately 10 times for X-type diodes [Fig. S6(d) in the Supplemental Material [62]]. The mechanisms for strain tuning these device performances, as mentioned previously, are mainly based on the strain tuning of the band structure (e.g., band gap) and other microscopic electronic transport characteristics (e.g., effective mass and carrier mobility). The results of strain-engineered (along the uniaxial y direction and biaxial xy direction) ScSI-monolayer p-n-junction diodes are also shown in Fig. S7 in the Supplemental Material [62], showing a similar device performance with the same mechanisms for strain tuning.

To further understand the outstanding rectifying effect and electronic transport properties of the two types of ScXI monolayer p-n-junction diodes, we further calculated and analyzed their transmission coefficients $T(E)$ and projected local density of states (PLDOS) under biases of 0, 1.0, and −1.0 V, as shown in Fig. 6. For the X-type ScSI-based diode, there was minimal electron transmission near E_F with an almost zero transmission coefficient at the 0 V bias [Fig. 6(a)], owing to the long electron tunneling path and high energy barrier, according to their PLDOS at the equilibrium state. When applying reverse bias across the p-n junction, such as −1.0 V, the bands of the p- and n-doped terminals shifted up and down accordingly, then band overlap occurred [Fig. 6(b)], leading to significant shortening of the tunneling path between the conduction bands of the D electrode and the valence bands of the S electrode. This facilitated direct electron tunneling with a large transmission coefficient within the bias window (BW) and thus generated tunneling current. In contrast, under forward bias, such as 1.0 V, the conductive and valence band states shifted upward and downward, respectively, and both were outside the BW, leading to a larger band gap. Therefore, electron tunneling between the two electrodes was forbidden, and the transmission coefficient remained zero owing to the band alignment, as depicted in Fig. 6(c). We also analyzed the electron transmission spectra $T(E, V)$ of the X-type p-n-junction diode of the ScSI monolayer, as shown in Fig. 6(d). Obviously, within the BW, electron transmissions only appeared in the reverse bias region and not in the forward bias range, which explains the I-V curve characteristics of the rectifying behavior. The Y-type diode has rectifying mechanisms similar to those of the X-type diode [Figs. 6(e)–6(h)], but with a smaller electron transmission, which corresponds to the electrical anisotropy of the ScSI monolayer. Figs. S8(a) and S8(d) in the Supplemental Material [62] display the k-dependent electron transmission coefficients $T(E, k)$ under -1.0 V. Within the BW, strong transmission was observed near the Γ point. For the X-type diode, the electron retained high transmission coefficients over the whole Brillouin zone, i.e., from Γ to Y $(-Y)$. However, for the Y-type diode, an electron transmission cloud with the shape of an airplane gradually decreased to almost zero from Γ to X $(-X)$, leading to a reduced transmission ability for the Y-type diode under a reverse bias range and the appearance of an electrical anisotropy behavior.

Diodes based on ScSeI, ScTeI, and strain-engineered ScSI (with 6% compressive strain along the x direction) monolayers have the same rectifying mechanisms, consistent with their I-V curve characteristics, and similar device characteristics to ScSI-based diodes (Figs. S8–S12 in the Supplemental Material [62]). Interestingly, the PLDOS of the ScTeI-based diode has a smaller gap between the valence and conduction bands than those of the diodes based on ScSI and ScSeI, which can better facilitate electron transmission and partly explain the generation of a larger current density. Furthermore, we observed that within the BW, more electrons in the region of high positive energies, instead of negative energies, have larger transmission coefficients for these two types of diodes based on ScXI monolayers as the chalcogen atoms move down from S to Te. Moreover, applying 6% compressive strain along the x direction on the ScSI monolayer induces significantly stronger electron transmission for the X-type diode and a much-reduced transmission ability for the Y-type diode.

D. Field-effect transistors of ScXI monolayers

The transmission performance of a device can also be enhanced using a vertical electric field. Therefore, we studied the field-effect properties of p-i-n-junction FETs constructed using ScXI monolayers, as shown in Fig. 7(a). The FET is comprised of electrodes on both sides, consisting of p- and n-doped ScXI monolayers with doping concentrations of 3×10^{13} cm^{-2}. The central intrinsic region (i) of approximately 3 nm, consisting of an intrinsic ScXI monolayer, acts as the FET channel and is covered by top and bottom gates that span the entire area. To determine the electron current flowing through the p-i-n-junction FET, the following equation was used:

$$I(V_b, V_g) = \frac{2e}{h} \int_{-\infty}^{\infty} T(E, V_b, V_g)[F_D(E - \mu_D) - F_S(E - \mu_S)]dE. \tag{3}$$

Figure 7(b) shows the I-V curves from –1.0 V to 1.0 V of both X-type and Y-type ScSI monolayer p-i-n-junction FETs under zero gate voltage (V_g). It can be seen that the ScSI-monolayer FET exhibits the same perfect rectifying effects with the same transport mechanisms (see Fig. S13 in the Supplemental Material [62]) and strong electrical anisotropy as the p-n-junction diode, but with a much smaller current density owing to the semiconductor nature of the central intrinsic region. When a positive gate voltage of 5 V was applied, the current density drastically decreased by almost 60 times [Fig. 7(c)], and its maximum was almost zero (approximately 0.06 mA mm^{-1}). In contrast, for V_g equal to 10 or –10 V, the currents dramatically increased and the threshold voltage for both X-type and Y-type FETs decreased to 0.5 from 0.7 V [Figs. 7(d) and 7(e)]. Moreover, the transmission behaviors are exactly the same for gate voltages of 10 and –10 V. To further investigate the field-effect characteristics of the p-i-n-junction FET, calculations of the I-V curves at various V_g values ranging from –10 to 10 V were performed. Figure 7(f) shows the current density at a bias of –1.0 V under different V_g conditions. It can be observed that the positive and negative gate voltages have a symmetrical impact on the FET. The current initially decreases to a minimum value at V_g of 4 or –4 V, and then rapidly and nearly linearly increases as the gate voltage is further increased. These findings indicate that the gate voltage effectively controlled the current flowing through the p-i-n-junctions, highlighting the exceptional field-effect behavior of the device.

The p-i-n-junction FETs based on ScSeI, ScTeI, and strain-engineered (with 6% compressive strain along x direction) ScSI monolayers also exhibited similar device characteristics to their corresponding p-n-junction diodes and the same excellent field-effect behavior as the ScSI-based p-i-n-junction FET (Figs. S14–S17 in the Supplemental Material [62]). When a positive or negative gate voltage was applied, the X-type p-i-n-junction FETs based on ScSeI and ScTeI yielded a significantly smaller threshold voltage (0.1 V) than the ScSI-based p-i-n-junction FET, as shown in Figs. S14(b)–S14(d) and S15(b)–S15(d) in

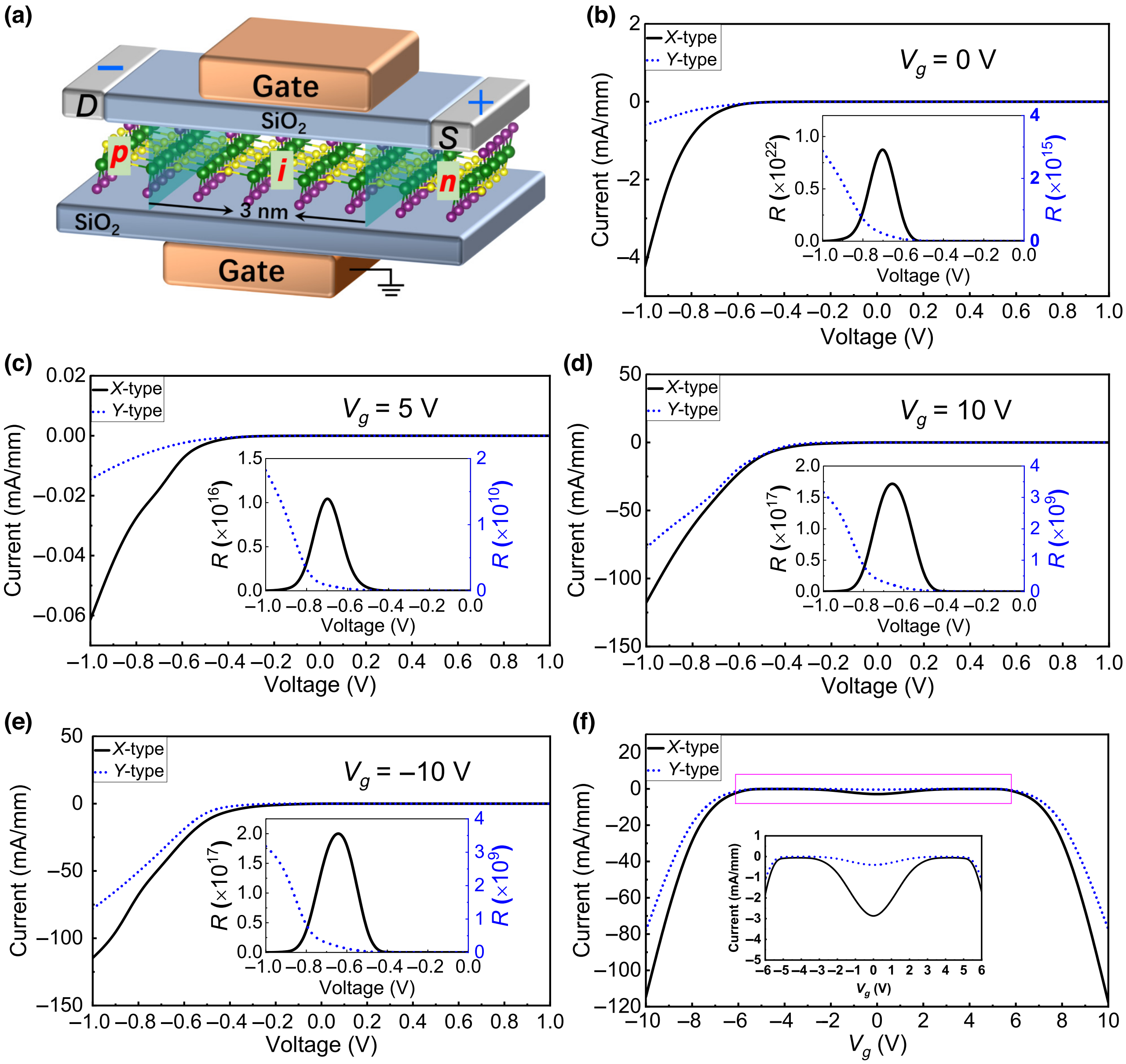

FIG. 7. Transport properties of the ScSI monolayer *p-i-n*-junction field-effect transistor (FET) with a doping concentration of 3×10^{13} cm^{-2}. (a) Schematic of the *p-i-n*-junction FET. (b)–(e) Bias-dependent current of the *p-i-n*-junction FET for the ScSI monolayer under gate voltages of 0, 5, 10, and −10 V, respectively. The rectification ratio *R* is shown in the insets of (b)–(e). (f) Distribution of the current of the *p-i-n*-junction FET at the bias of −1 V under different gate voltages for the ScSI monolayer.

the Supplemental Material [62]. Simultaneously, the rectification ratio improved as the gate voltage increased. Both X-type and Y-type FETs based on ScTeI and strain-engineered ScSI monolayers induced a much higher current density than those based on ScSI monolayers at the same bias voltage and gate voltage, yielding stronger electrical anisotropy, similar to their *p-n* junctions (Figs. S15 and S16 in the Supplemental Material [62]). In addition, the subthreshold swing (SS) is a crucial parameter for evaluating the performance of FET devices as it has a direct impact on energy consumption and switching speed [76–79]. We investigated the SSs of the FETs, as shown in Fig. S18 in the Supplemental Material [62]. Note the SS of each FET is larger than those of the WSi_2N_4 FETs [24] and carbon nanotube Dirac source FETs [76], which means that the FETs investigated here would not be useful as logical switches.

E. Phototransistors of ScXI monolayers

Furthermore, we investigated the optical properties and photoelectric performance of the ScXI monolayers.

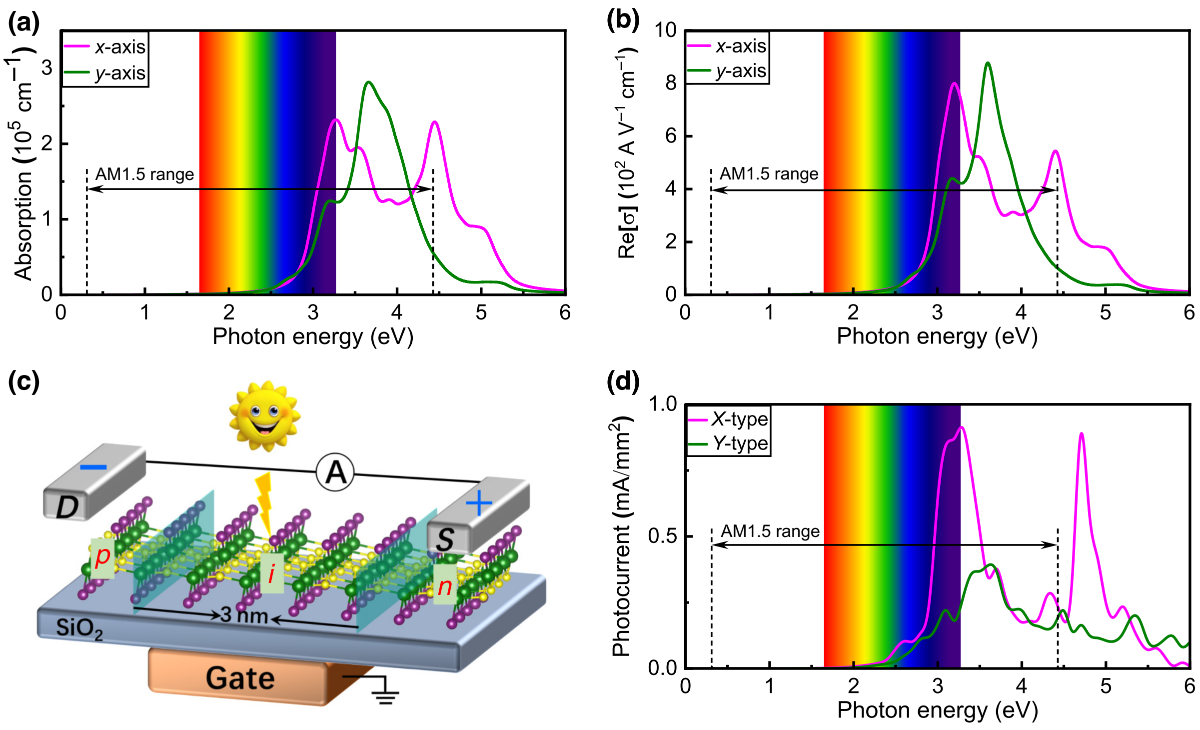

FIG. 8. Photoelectric properties of the ScSI monolayer. (a) Optical absorption coefficient and (b) real part of optical conductivity of the ScSI monolayer. (c) Schematic of the *p-i-n*-junction phototransistor of the ScSI monolayer. (d) Intrinsic photocurrent density of the *p-i-n*-junction phototransistor of the ScSI monolayer under zero bias (without power) and zero V_g.

The optical conductivity, complex refractive index, and absorption coefficient were calculated as follows [80]:

$$\sigma = -i\omega\varepsilon_0\chi(\omega),\, n + i\kappa = \sqrt{1 + i\frac{\sigma}{\varepsilon_0\omega}},\, \alpha = 2\frac{\omega}{c}\kappa, \quad (4)$$

where ω is the frequency of the electromagnetic waves, ε_0 represents the electrical constant, $\chi(\omega)$ is the susceptibility tensor, $\kappa(\omega)$ is the extinction coefficient, and c is the speed of light. The susceptibility tensor $\chi(\omega)$ was calculated by the Kubo-Greenwood formula as follows [81]:

$$\chi_{ij}(\omega) = -\frac{e^2\hbar^4}{m^2\varepsilon_0 V\omega^2}\sum_{nm}\frac{F(E_m) - F(E_n)}{E_{mn} - \hbar\omega - i\Gamma}\pi^i_{nm}\pi^j_{nm}, \quad (5)$$

where V is the volume, F is the Fermi-Dirac function, Γ is the broadening, and π^i_{nm} is the ith dipole matrix element between the states n and m. Figure 8(a) displays the optical absorption spectra of the ScSI monolayer. It can be seen that the absorption coefficient curves begin to rise from zero at a photon energy of approximately 2.4 eV, which corresponds to its electronic band gap (2.421 eV). Simultaneously, photoconduction is initiated [Fig. 8(b)]. There are two main peaks around 3.27 and 4.44 eV along the x axis corresponding to the purple and ultraviolet regions, respectively, and one main peak around 3.65 eV (UR) along the y axis in the optical conductivity curves. The peaks in the conductivity curves are consistent with the high peaks (up to 10^5 cm^{-1}) of the absorption coefficients. These results demonstrate the sensitive photoresponse and anisotropic optical behavior of the ScSI monolayer.

A phototransistor was constructed using a *p-i-n*-junction consisting of a ScSI monolayer, as depicted in Fig. 8(c). Furthermore, the characteristics of the phototransistor response to linearly polarized light were investigated. Within this analysis, the absorption of photons with frequency ω was considered, resulting in a first-order correction to the photogenerated current at electrode γ (γ is D or S). The formula used to derive the current was [82,83]

$$I_\gamma = \frac{e}{h}\int_{-\infty}^{\infty}\sum_{\beta=D,S}[1 - F_\gamma(E)]F_\beta(E - \hbar\omega)T^-_{\gamma,\beta}(E) - F_\gamma(E)[1 - F_\beta(E + \hbar\omega)]T^+_{\gamma,\beta}(E)dE. \quad (6)$$

Figure 8(d) shows the intrinsic photocurrent curves of the *p-i-n*-junction phototransistor of the ScSI monolayer with a doping concentration of 3×10^{13} cm^{-2} under zero bias (without power) and zero V_g. The X-type *p-i-n*-junction phototransistor of the ScSI monolayer had a good photoelectric response in the purple light and URs

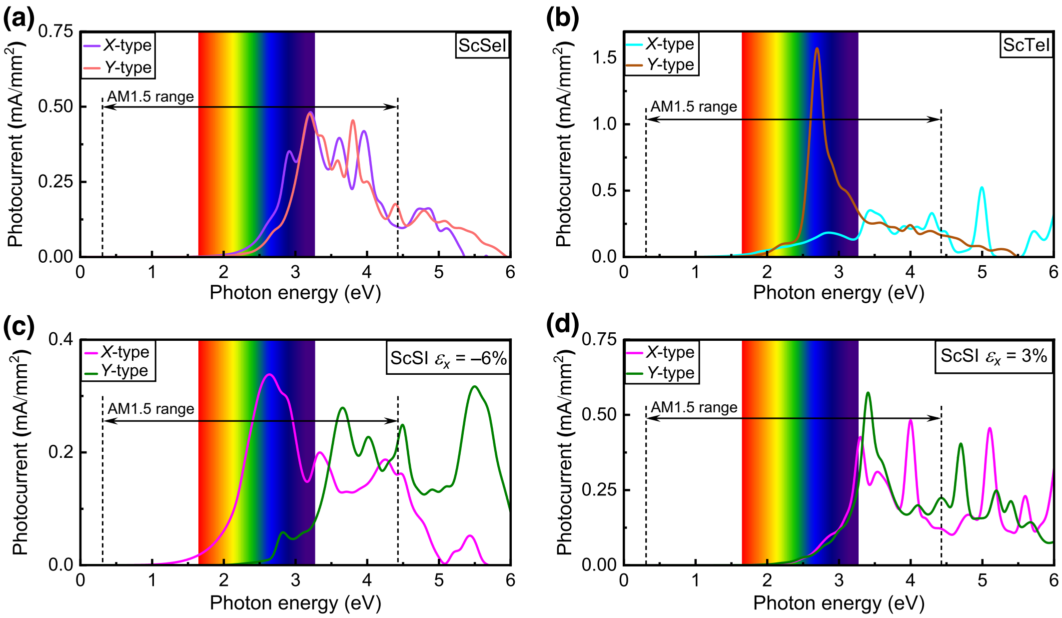

FIG. 9. Intrinsic photocurrent density of the *p*-*i*-*n*-junction phototransistor of the (a) ScSeI monolayer, (b) ScTeI monolayer, and ScSI monolayer under (c) 6% compressive and (d) 3% tensile strain along the *x* direction under zero bias (without power) and zero V_g.

because of its large optical conductivity in these regions, as two strong photocurrent peaks were observed. Therefore, it can be used as a photodetector to detect purple and ultraviolet light. In addition, within the AM1.5 standard [84], its total photocurrent density was as high as 0.91 mA mm^{-2}, which is similar to the silicon solar-cell device [82], demonstrating its potential application in photovoltaic devices. For the case of the *Y*-type *p*-*i*-*n*-junction phototransistor of the ScSI monolayer, a photocurrent peak was also observed in the UR with a smaller total photocurrent (0.39 mA mm^{-2}), also revealing the anisotropic photoelectric properties of the ScSI monolayer.

Compared with ScSI, the positions of the absorption edge and absorption peaks of the ScSeI and ScTeI monolayers were located in the lower photon energy region because of their smaller energy gap [Figs. S19(a) and S19(b) in the Supplemental Material [62]]. Meanwhile, their photoconduction processes were also opened at a lower photon energy of 2.0 V (1.65 V) for the ScSeI (ScTeI) monolayer [Figs. S19(c) and S19(d) in the Supplemental Material [62]]. In addition, Fig. 9(a) shows that the ScSeI monolayer exhibited weak anisotropic photoelectric properties. However, the total photocurrent excited by the *X*-type *p*-*i*-*n*-junction phototransistor of the ScTeI monolayer was significantly smaller than that of the *Y*-type phototransistor, exhibiting strong anisotropic photoelectric properties, as shown in Fig. 9(b). In particular, the *Y*-type *p*-*i*-*n*-junction phototransistor of the ScTeI monolayer generated a sharp photocurrent peak (up to 1.57 mA mm^{-2}) in the blue light region, demonstrating its potential use as a photodetector for detecting blue light. These exciting photoelectronic properties render the Sc*X*I monolayer a promising material for photovoltaic devices and photoelectric sensors.

Furthermore, the applied strain significantly influenced the photoelectric properties of the ScSI monolayer. Applying 6% compressive strain along *x* direction on the ScSI monolayer led to a wider absorbing range and a slight decrease of absorption coefficient and optical conductivity in the visible-light region along the *x* axis [Figs. S20(a) and S20(c) in the Supplemental Material [62]]. The absorption and photoconduction processes were initiated earlier because of the decrease of the band gap induced by strain. Its phototransistor had a good photoresponse to almost the entire visible and ultraviolet regions, and excited a slightly smaller total photocurrent (0.34 mA mm^{-2}) as a photocurrent peak in the blue light region within the AM1.5 range [84], as shown in Fig. 9(c). In addition, when a 3% tensile strain was applied along the *x* direction on the ScSI monolayer, its light absorption and photoconductivity peaks shifted toward higher energy and fell within the ultraviolet region, as shown in Figs. S20(b) and S20(d) in the Supplemental Material [62], because of the widening of the electronic band gap induced by the strain. Therefore, the peaks of the photocurrent for its phototransistor also shifted toward higher energy and fell within the ultraviolet region, as shown in Fig. 9(d), which broadens its application scope in ultraviolet detection. These results demonstrate that the photoelectric properties of the ScSI monolayer can be adjusted by introducing a strain.

To investigate the regulation effect from the gate electrode on the photoelectric performance of the phototransistor, we also calculated the photocurrent spectra of the X-type p-i-n-junction phototransistor of the ScSI monolayer under gate voltages from -6 to 6 V, as shown in Fig. S21(a) in the Supplemental Material [62]. Under the AM1.5 standard [84], the application of gate voltages reduced the photoelectric performance and should be avoided in photovoltaic devices. For the Y-type p-i-n-junction phototransistor, the photocurrent within the UR was enhanced under a positive small gate voltage of 1.5 V [Fig. S21(b) in the Supplemental Material [62]]. For the cases of ScSeI, ScTeI, and ScSI under 6% compressive strain along the x direction, the results are shown in the Figs. S21(c)–S21(h) in the Supplemental Material [62]. These results demonstrate that the application of gate voltage can influence the photoexcited current and has a regulatory effect on the photoelectric performance of the ScXI-based p-i-n-junction phototransistor.

IV. CONCLUSIONS

In summary, we designed several conceptual nanodevices based on ScXI monolayers and theoretically investigated their electronic, mechanical, transport, and photoelectric properties, as well as strain engineering to tune these properties. The results demonstrated that the 2D ScXI semiconductors with a moderate direct band gap of $2.42 - 1.34$ eV were dynamically, thermally, and mechanically stable. The ScXI monolayers exhibited significant mechanical anisotropy and relatively low stiffness. The electronic properties of the ScSI monolayer were sensitive to the applied uniaxial and biaxial strains. Strain has been predicted to be an efficient way to engineer the band gap as well as the effective mass. Both X-type and Y-type p-n-junction diodes of ScXI monolayers showed a strong rectifying effect with an ultrahigh rectifying ratio (up to a magnitude of 1020 for ScSI), large current density (up to 319.45 mA mm^{-1} for ScTeI), and remarkable electrical anisotropy with a large current anisotropy ratio ($\eta = 9.65$ for ScTeI). The ScXI-monolayer FETs exhibited the same perfect rectifying effects and strong electrical anisotropy as the p-n-junction diode. Moreover, the gate voltage could effectively regulate the current through the FET. The ScXI monolayers and their phototransistors also showed good photoelectric responses in the visible and ultraviolet regions. The ScXI monolayers from S to Te also exhibited different device performances. These results demonstrate the potential applications of ScXI monolayers in functional electronic and photoelectric devices. Furthermore, a 6% compressive strain along the x direction can tune the device transport and photoelectric properties of the ScSI monolayer, such as larger current density, stronger electrical anisotropy, lower threshold voltage, and a wider visible-light absorption band. Strain engineering may be a promising method to modify the electrical transport and photoelectric properties of ScSI monolayer, with the potential to achieve high-performance devices. Because of their strain-tunable band gap, excellent electronic transport, and photoelectric properties, ScXI monolayers are expected to be applied in nanodevices and optoelectronic devices.

ACKNOWLEDGEMENTS

We acknowledge funding from the National Natural Science Foundation of China (Grants No. 12274117, No. 62274066, and No. 62275074), the Natural Science Foundation of Henan Province (Grant No. 242300421214), the Young Top-notch Talents Project of Henan Province (2021 year), the Program for Innovative Research Team (in Science and Technology) in University of Henan Province (Grant No. 24IRTSTHN025), the Key Scientific Project of Universities of Henan Province (Grant No. 22A140020), and Henan Center for Outstanding Overseas Scientists (Grant No. GZS2023007). We thank the High Performance Computing Center of Henan Normal University.

[1] S. Wang, X. Liu, and P. Zhou, The road for 2D semiconductors in the silicon age, Adv. Mater. **34**, 2106886 (2022).

[2] K. S. Novoselov, A. K. Geim, S. V. Morozov, D. Jiang, Y. Zhang, S. V. Dubonos, I. V. Grigorieva, and A. A. Firsov, Electric field effect in atomically thin carbon films, Science **306**, 666 (2004).

[3] Q. H. Wang, K. Kalantar-Zadeh, A. Kis, J. N. Coleman, and M. S. Strano, Electronics and optoelectronics of two-dimensional transition metal dichalcogenides, Nat. Nanotechnol. **7**, 699 (2012).

[4] M. Chhowalla, H. S. Shin, G. Eda, L.-J. Li, K. P. Loh, and H. Zhang, The chemistry of two-dimensional layered transition metal dichalcogenide nanosheets, Nat. Chem. **5**, 263 (2013).

[5] Y. An, M. Zhang, D. Wu, Z. Fu, and K. Wang, The electronic transport properties of transition-metal dichalcogenide lateral heterojunctions, J. Mater. Chem. C **4**, 10962 (2016).

[6] S. Manzeli, D. Ovchinnikov, D. Pasquier, O. V. Yazyev, and A. Kis, 2D transition metal dichalcogenides, Nat. Rev. Mater. **2**, 17033 (2017).

[7] T. Chowdhury, E. C. Sadler, and T. J. Kempa, Progress and prospects in transition-metal dichalcogenide research beyond 2D, Chem. Rev. **120**, 12563 (2020).

[8] E. C. Regan, D. Wang, E. Y. Paik, Y. Zeng, L. Zhang, J. Zhu, A. H. MacDonald, H. Deng, and F. Wang, Emerging exciton physics in transition metal dichalcogenide heterobilayers, Nat. Rev. Mater. **7**, 778 (2022).

[9] D. Pacilé, J. C. Meyer, Ç. Ö. Girit, and A. Zettl, The two-dimensional phase of boron nitride: Few-atomic-layer sheets and suspended membranes, Appl. Phys. Lett. **92**, 133107 (2008).

[10] L. Song, L. Ci, H. Lu, P. B. Sorokin, C. Jin, J. Ni, A. G. Kvashnin, D. G. Kvashnin, J. Lou, B. I. Yakobson,

et al., Large scale growth and characterization of atomic hexagonal boron nitride layers, Nano Lett. **10**, 3209 (2010).

[11] L. Li, Y. Yu, G. J. Ye, Q. Ge, X. Ou, H. Wu, D. Feng, X. H. Chen, and Y. Zhang, Black phosphorus field-effect transistors, Nat. Nanotechnol. **9**, 372 (2014).

[12] M. Liu, S. Feng, Y. Hou, S. Zhao, L. Tang, J. Liu, F. Wang, and B. Liu, High yield growth and doping of black phosphorus with tunable electronic properties, Mater. Today **36**, 91 (2020).

[13] B. Anasori, M. R. Lukatskaya, and Y. Gogotsi, 2D metal carbides and nitrides (MXenes) for energy storage, Nat. Rev. Mater. **2**, 16098 (2017).

[14] Y. Gogotsi and B. Anasori, The rise of MXenes, ACS Nano **13**, 8491 (2019).

[15] Y. Deng, Y. Yu, M. Z. Shi, Z. Guo, Z. Xu, J. Wang, X. H. Chen, and Y. Zhang, Quantum anomalous Hall effect in intrinsic magnetic topological insulator $MnBi_2Te_4$, Science **367**, 895 (2020).

[16] Y. An, K. Wang, S. Gong, Y. Hou, C. Ma, M. Zhu, C. Zhao, T. Wang, S. Ma, H. Wang, *et al.*, Nanodevices engineering and spin transport properties of $MnBi_2Te_4$ monolayer, npj Comput. Mater. **7**, 45 (2021).

[17] B. Radisavljevic, A. Radenovic, J. Brivio, V. Giacometti, and A. Kis, Single-layer MoS_2 transistors, Nat. Nanotechnol. **6**, 147 (2011).

[18] M. Chhowalla, D. Jena, and H. Zhang, Two-dimensional semiconductors for transistors, Nat. Rev. Mater. **1**, 16052 (2016).

[19] Y. An, Y. Hou, K. Wang, S. Gong, C. Ma, C. Zhao, T. Wang, Z. Jiao, H. Wang, R. Wu, Multifunctional lateral transition-metal disulfides heterojunctions, Adv. Funct. Mater. **30**, 2002939 (2020).

[20] F. Wu, H. Tian, Y. Shen, Z. Hou, J. Ren, G. Gou, Y. Sun, Y. Yang, and T.-L. Ren, Vertical MoS_2 transistors with sub-1-nm gate lengths, Nature **603**, 259 (2022).

[21] J. Jiang, L. Xu, C. Qiu, and L.-M. Peng, Ballistic two-dimensional InSe transistors, Nature **616**, 470 (2023).

[22] Q. Liu, J.-J. Li, D. Wu, X.-Q. Deng, Z.-H. Zhang, Z.-Q. Fan, and K.-Q. Chen, Gate-controlled reversible rectifying behavior investigated in a two-dimensional MoS_2 diode, Phys. Rev. B **104**, 045412 (2021).

[23] S. Gopalan, M. L. Van de Put, G. Gaddemane, and M. V. Fischetti, Theoretical study of electronic transport in two-dimensional transition metal dichalcogenides: effects of the dielectric environment, Phys. Rev. Appl. **18**, 054062 (2022).

[24] Y. Li, C. Qi, X. Zhou, L. Xu, Q. Li, S. Liu, C. Yang, S. Liu, L. Xu, J. Dong, *et al.*, Monolayer WSi_2N_4: A promising channel material for sub-5-nm-gate homogeneous CMOS devices, Phys. Rev. Appl. **20**, 064044 (2023).

[25] Y. Pan, L. Zhang, L. Huang, L. Li, L. Meng, M. Gao, Q. Huan, X. Lin, Y. Wang, S. Du, *et al.*, Construction of 2D atomic crystals on transition metal surfaces: Graphene, silicene, and hafnene, Small **10**, 2215 (2014).

[26] H. Suzuki, N. Ogura, T. Kaneko, and T. Kato, Highly stable persistent photoconductivity with suspended graphene nanoribbons, Sci. Rep. **8**, 11819 (2018).

[27] Q. Zhou, Q. Chen, Y. Tong, and J. Wang, Light-induced ambient degradation of few-layer black phosphorus: Mechanism and protection, Angew. Chem., Int. Ed. **55**, 11437 (2016).

[28] Z. Yu, Z.-Y. Ong, Y. Pan, Y. Cui, R. Xin, Y. Shi, B. Wang, Y. Wu, T. Chen, Y.-W. Zhang, *et al.*, Realization of room-temperature phonon-limited carrier transport in monolayer MoS_2 by dielectric and carrier screening, Adv. Mater. **28**, 547 (2016).

[29] Y. Wang, J. C. Kim, R. J. Wu, J. Martinez, X. Song, J. Yang, F. Zhao, A. Mkhoyan, H. Y. Jeong, and M. Chhowalla, Van der Waals contacts between three-dimensional metals and two-dimensional semiconductors, Nature **568**, 70 (2019).

[30] H. Qi, Z. Sun, C. Shen, Z. Chang, Z. Wang, X. Wang, M. Zhang, and N. Wang, High thermoelectric performance of $Al_2X_2Se_2$ ($X = Cl$, Br, I) monolayers with strong anisotropy in lattice thermal conductivity, ACS Appl. Energy Mater. **5**, 7371 (2022).

[31] H. Qi, Z. Sun, N. Wang, G. Qin, H. Zhang, and C. Shen, Two-dimensional $Al_2I_2Se_2$: A promising anisotropic thermoelectric material, J. Alloys Compd. **876**, 160191 (2021).

[32] N. Miao, B. Xu, L. Zhu, J. Zhou, and Z. Sun, 2D Intrinsic ferromagnets from van der Waals antiferromagnets, J. Am. Chem. Soc. **140**, 2417 (2018).

[33] Y. Guo, Y. Zhang, S. Yuan, B. Wang, and J. Wang, Chromium sulfide halide monolayers: Intrinsic ferromagnetic semiconductors with large spin polarization and high carrier mobility, Nanoscale **10**, 18036 (2018).

[34] B. Xu, S. Li, K. Jiang, J. Yin, Z. Liu, Y. Cheng, and W. Zhong, Switching of the magnetic anisotropy via strain in two dimensional multiferroic materials: CrSX ($X = Cl$, Br, I), Appl. Phys. Lett. **116**, 052403 (2020).

[35] Y. Gao, Q. Liu, Y. Zhu, X. Jiang, and J. Zhao, Magnetic field modulated photoelectric devices in ferromagnetic semiconductor CrXh ($X = S/Se$, $h = Cl/Br/I$) van der Waals heterojunctions, Appl. Phys. Lett. **119**, 032103 (2021).

[36] S. W. Jang, D. H. Kiem, J. Lee, Y.-G. Kang, H. Yoon, and M. J. Han, Hund's physics and the magnetic ground state of CrOX ($X = Cl$, Br), Phys. Rev. Mater. **5**, 034409 (2021).

[37] D. J. Rizzo, A. S. McLeod, C. Carnahan, E. J. Telford, A. H. Dismukes, R. A. Wiscons, Y. Dong, C. Nuckolls, C. R. Dean, A. N. Pasupathy, *et al.*, Visualizing atomically layered magnetism in CrSBr, Adv. Mater. **34**, 2201000 (2022).

[38] E. J. Telford, A. H. Dismukes, R. L. Dudley, R. A. Wiscons, K. Lee, D. G. Chica, M. E. Ziebel, M.-G. Han, J. Yu, S. Shabani, *et al.*, Coupling between magnetic order and charge transport in a two-dimensional magnetic semiconductor, Nat. Mater. **21**, 754 (2022).

[39] Y. Wang, N. Luo, J. Zeng, L.-M. Tang, and K.-Q. Chen, Magnetic anisotropy and electric field induced magnetic phase transition in the van der Waals antiferromagnet CrSBr, Phys. Rev. B **108**, 054401 (2023).

[40] C. Wang, X. Zhou, L. Zhou, N.-H. Tong, Z.-Y. Lu, and W. Ji, A family of high-temperature ferromagnetic monolayers with locked spin-dichroism-mobility anisotropy: MnNX and CrCX ($X = Cl$, Br, I; $C = S$, Se, Te), Sci. Bull. **64**, 293 (2019).

[41] M. Hu, S. Xu, C. Liu, G. Zhao, J. Yu, and W. Ren, First-principles prediction of a room-temperature ferromagnetic and ferroelastic 2D multiferroic MnNX ($X = F$, Cl, Br, and I), Nanoscale **12**, 24237 (2020).

[42] J. Pan, J. Yu, Y.-F. Zhang, S. Du, A. Janotti, C.-X. Liu, and Q. Yan, Quantum anomalous Hall effect in two-dimensional

magnetic insulator heterojunctions, npj Comput. Mater. **6,** 152 (2020).

[43] Y. Zou, X. Wang, L. Liu, T. Song, Z. Liu, and X. Cui, First-principles study on mechanical, electronic, and magnetic properties of room temperature ferromagnetic half-metal MnNCl monolayer, Nanomaterials **13,** 1712 (2023).

[44] T. Zhang, Y. Wang, H. Li, F. Zhong, J. Shi, M. Wu, Z. Sun, W. Shen, B. Wei, W. Hu, *et al.*, Magnetism and optical anisotropy in van der Waals antiferromagnetic insulator CrOCl, ACS Nano **13,** 11353 (2019).

[45] S.-Z. Huang, Q.-Y. Feng, B.-Y. Wang, H.-D. Yang, B. Li, X. Xiang, X.-T. Zu, and H.-X. Deng, Valley degeneracy-enhanced thermoelectric performance in in-based FeOCl-type monolayers, ACS Appl. Energy Mater. **5,** 13042 (2022).

[46] X. Song, X. Chen, G. Wang, L. Zhou, H. Yang, X. Li, H. Yang, Y. Shen, Y. Luo, and N. Wang, Strong anisotropy of $Sc_2X_2Se_2$ (X = Cl, Br, I) monolayers contributes to high thermoelectric performance, Phys. Chem. Chem. Phys. **25,** 24332 (2023).

[47] Y. Lu and J. H. Warner, Synthesis and applications of wide bandgap 2D layered semiconductors reaching the green and blue wavelengths, ACS Appl. Electron. Mater. **2,** 1777 (2020).

[48] A. M. Ferrenti, M. A. Siegler, S. Gao, N. Ng, and T. M. McQueen, ScSI: A new exfoliatable semiconductor, Chem. Mater. **34,** 5443 (2022).

[49] B. Li, Y. Yang, H. Qi, Z. Sun, F. Yang, K. Huang, Z. Chen, B. He, X. Xiao, C. Shen, *et al.*, Monolayer $Sc_2I_2S_2$: An excellent n-type thermoelectric material with significant anisotropy, ACS Appl. Energy Mater. **5,** 7230 (2022).

[50] L. Hou, L. Dong, P. Shi, J. Su, Y. Tu, Y. Zhang, and B. Wang, Density functional theory study of layer-controlled band gap and strong anisotropic properties in ScSI nanosheet: implications for photoelectric sensor, ACS Appl. Nano Mater. **6,** 14621 (2023).

[51] M. Brandbyge, J.-L. Mozos, P. Ordejón, J. Taylor, and K. Stokbro, Density-functional method for nonequilibrium electron transport, Phys. Rev. B **65,** 165401 (2002).

[52] S. Smidstrup, T. Markussen, P. Vancraeyveld, J. Wellendorff, J. Schneider, T. Gunst, B. Verstichel, D. Stradi, P. A. Khomyakov, U. G. Vej-Hansen, *et al.*, QuantumATK: An integrated platform of electronic and atomic-scale modelling tools, J. Phys.: Condens. Matter **32,** 015901 (2020).

[53] J. P. Perdew, K. Burke, and M. Ernzerhof, Generalized gradient approximation made simple, Phys. Rev. Lett. **77,** 3865 (1996).

[54] S. Grimme, J. Antony, S. Ehrlich, and H. Krieg, A consistent and accurate *ab initio* parametrization of density functional dispersion correction (DFT-D) for the 94 elements H-Pu, J. Chem. Phys. **132,** 154104 (2010).

[55] S. Grimme, S. Ehrlich, and L. Goerigk, Effect of the damping function in dispersion corrected density functional theory, J. Comput. Chem. **32,** 1456 (2011).

[56] M. Schlipf and F. Gygi, Optimization algorithm for the generation of ONCV pseudopotentials, Comput. Phys. Commun. **196,** 36 (2015).

[57] H. J. Monkhorst and J. D. Pack, Special points for Brillouin-zone integrations, Phys. Rev. B **13,** 5188 (1976).

[58] K. Wang, R. Xiao, T. Yang, Y. Zeng, and X. Tan, The electronic structure and interfacial contact with metallic borophene of monolayer ScSX (X = I, Br, and Cl), Phys. Chem. Chem. Phys. **25,** 232 (2023).

[59] L. Rao, G. Tang, and J. Hong, Electronic and mechanical properties of ScXI (X = S, Se) monolayers and their heterostructures, Phys. Rev. Mater. **7,** 014010 (2023).

[60] R. Zacharia, H. Ulbricht, and T. Hertel, Interlayer cohesive energy of graphite from thermal desorption of polyaromatic hydrocarbons, Phys. Rev. B **69,** 155406 (2004).

[61] S. Sarikurt, T. Kocabaş, and C. Sevik, High-throughput computational screening of 2D materials for thermoelectrics, J. Mater. Chem. A **8,** 19674 (2020).

[62] See the Supplemental Material at http://link.aps.org/supplemental/10.1103/PhysRevApplied.21.054053 for Figs. S1–S21, Table S1, and calculation methods for the orientation-dependent elastic moduli and the effective mass $m_{e(h)}{}^*$ of carriers.

[63] S. Singh, L. Lang, V. Dovale-Farelo, U. Herath, P. Tavadze, F.-X. Coudert, and A. H. Romero, MechElastic: A Python library for analysis of mechanical and elastic properties of bulk and 2D materials, Comput. Phys. Commun. **267,** 108068 (2021).

[64] M. Born and K. Huang, *Dynamic Theory of Crystal Lattice, Clarendon* (Oxford University Press, Oxford, 1954).

[65] V. Wang, G. Tang, Y.-C. Liu, R.-T. Wang, H. Mizuseki, Y. Kawazoe, J. Nara, and W. T. Geng, High-throughput computational screening of two-dimensional semiconductors, J. Phys. Chem. Lett. **13,** 11581 (2022).

[66] X. Xu, Y. Ma, T. Zhang, C. Lei, B. Huang, and Y. Dai, Prediction of two-dimensional antiferromagnetic ferroelasticity in an AgF_2 monolayer, Nanoscale Horiz. **5,** 1386 (2020).

[67] C. Si, Z. Sun, and F. Liu, Strain engineering of graphene: A review, Nanoscale **8,** 3207 (2016).

[68] S. Deng, A. V. Sumant, and V. Berry, Strain engineering in two-dimensional nanomaterials beyond graphene, Nano Today **22,** 14 (2018).

[69] Z. Dai, L. Liu, and Z. Zhang, Strain engineering of 2D materials: Issues and opportunities at the interface, Adv. Mater. **31,** 1805417 (2019).

[70] J. Du, H. Yu, B. Liu, M. Hong, Q. Liao, Z. Zhang, and Y. Zhang, Strain engineering in 2D material-based flexible optoelectronics, Small Methods **5,** 2000919 (2021).

[71] Y. Qi, M. A. Sadi, D. Hu, M. Zheng, Z. Wu, Y. Jiang, and Y. P. Chen, Recent progress in strain engineering on van der Waals 2D materials: Tunable electrical, electrochemical, magnetic, and optical properties, Adv. Mater. **35,** 2205714 (2023).

[72] D. Stradi, U. Martinez, A. Blom, M. Brandbyge, and K. Stokbro, General atomistic approach for modeling metal-semiconductor interfaces using density functional theory and nonequilibrium Green's function, Phys. Rev. B **93,** 155302 (2016).

[73] M. Büttiker, Y. Imry, R. Landauer, and S. Pinhas, Generalized many-channel conductance formula with application to small rings, Phys. Rev. B **31,** 6207 (1985).

[74] Y. An, M. Zhang, D. Wu, T. Wang, Z. Jiao, C. Xia, Z. Fu, and K. Wang, The rectifying and negative differential resistance effects in graphene/h-BN nanoribbon heterojunctions, Phys. Chem. Chem. Phys. **18,** 27976 (2016).

[75] J. Chen, Y. Guo, C. Ma, S. Gong, C. Zhao, T. Wang, X. Dong, Z. Jiao, S. Ma, G. Xu, *et al.*, Magnetic nanodevices and spin-transport properties of a two-dimensional CrSCl monolayer, Phys. Rev. Appl. **19**, 054013 (2023).

[76] C. Qiu, F. Liu, L. Xu, B. Deng, M. Xiao, J. Si, L. Lin, Z. Zhang, J. Wang, H. Guo, *et al.*, Dirac-source field-effect transistors as energy-efficient, high-performance electronic switches, Science **361**, 387 (2018).

[77] S. Salahuddin, K. Ni, and S. Datta, The era of hyper-scaling in electronics, Nat. Electron. **1**, 442 (2018).

[78] J. Lyu, J. Pei, Y. Guo, J. Gong, and H. Li, A new opportunity for 2D van der Waals heterostructures: Making steep-slope transistors, Adv. Mater. **32**, 1906000 (2020).

[79] X. Sun, C. Zhu, H. Liu, B. Zheng, Y. Liu, J. Yi, L. Fang, Y. Liu, X. Wang, M. Zubair, *et al.*, Contact and injection engineering for low SS reconfigurable FETs and high gain complementary inverters, Sci. Bull. **65**, 2007 (2020).

[80] R. M. Martin, *Electronic Structure: Basic Theory and Practical Methods* (Cambridge University Press, Cambridge, 2020).

[81] J. E. Sipe and E. Ghahramani, Nonlinear optical response of semiconductors in the independent-particle approximation, Phys. Rev. B **48**, 11705 (1993).

[82] M. Palsgaard, T. Markussen, T. Gunst, M. Brandbyge, and K. Stokbro, Efficient first-principles calculation of phonon-assisted photocurrent in large-scale solar-cell devices, Phys. Rev. Appl. **10**, 014026 (2018).

[83] L. Zhang, K. Gong, J. Chen, L. Liu, Y. Zhu, D. Xiao, and H. Guo, Generation and transport of valley-polarized current in transition-metal dichalcogenides, Phys. Rev. B **90**, 195428 (2014).

[84] G. ASTM, 173-03, *Terrestrial Reference Spectra for Photovoltaic Performance Evaluation* (American Society for Testing Materials (ASTM) International, West Conshohocken, 2012).